THE ASTROPHYSICAL JOURNAL, 532:970–979, 2000 April 1

THE X-RAY LINE EMISSION FROM THE SUPERNOVA REMNANT W49B

UNA HWANG,[1,2] ROBERT PETRE,[1] AND JOHN P. HUGHES[3]
Received 1999 July 21; accepted 1999 November 22

ABSTRACT

The Galactic supernova remnant W49B has one of the most impressive X-ray emission-line spectra obtained with *ASCA*. We use both plasma line diagnostics and broadband model fits to show that the Si and S emission lines require multiple spectral components. The spectral data do not necessarily require individual elements to be spatially stratified, as suggested by earlier work, although when *ASCA* line images are considered, it is possible that Fe is stratified with respect to Si and S. Most of the X-ray–emitting gas is from ejecta, based on the element abundances required, but is surprisingly close to being in collisional ionization equilibrium. A high ionization age implies a high internal density in a young remnant. The fitted emission measure for W49B indicates a minimum density of 2 cm^{-3}, with the true density likely to be significantly higher. W49B probably had a Type Ia progenitor, based on the relative element abundances, although a low-mass Type II progenitor is still possible. We find persuasive evidence for Cr and possibly Mn emission in the *ASCA* spectrum—the first detection of these elements in X-rays from a cosmic source.

Subject headings: supernova remnants — X-rays: ISM

1. INTRODUCTION

When the Galactic supernova remnant W49B (G43.3 − 0.2) was first detected as an X-ray source by the *Einstein Observatory*, its centrally bright morphology raised speculations that its X-ray emission is produced by nonthermal synchrotron processes (Pye et al. 1984), as in the Crab. The subsequent discovery of a prominent Fe K emission-line blend with *EXOSAT* showed that the X-ray emission is thermal and probably dominated by supernova ejecta (Smith et al. 1985). The *Advanced Satellite for Cosmology and Astronomy* (*ASCA*) has since provided the highest quality X-ray spectral data yet available for W49B, revealing a spectacular array of prominent emission lines from the elements Si, S, Ar, Ca, and Fe.

Fujimoto et al. (1995) analyzed the intensity ratios of the Lyα and Heα lines ($n = 2 \rightarrow n = 1$ transitions in the H- and He-like ions, respectively) using the *ASCA* data and concluded that the elements Si, S, Ar, and Ca cannot have the same average ionization age for a given temperature, with Si and S having the largest discrepancies. With the ionization age defined as the product $n_e t$ of the ambient electron density n_e and the time t since the gas was shock-heated (Gorenstein, Harnden, & Tucker 1974), this implies that each element either has a different density or was shocked at a different time. This result is important, if true, since all the elements Si, S, Ar, and Ca occupy essentially the same spatial zones in supernova models, while Fe initially occupies a spatial zone interior to these elements (e.g., Nomoto et al. 1997a; Thielemann, Nomoto, & Hashimoto 1990). The *ASCA* X-ray images of the remnant in emission lines of Si, S, and Fe (with a low spatial resolution of FWHM $> 1'$) suggest that the Si and S emission is distributed outside more centrally peaked continuum (4–6 keV) and Fe K emission. These results are interpreted as evidence for stratification of the supernova ejecta, with the Fe ejecta lying interior to the Si and S ejecta.

In this paper, we reexamine the *ASCA* data for W49B, carrying out a more complete and careful analysis of the X-ray line emission. We examine evidence for emission from less abundant elements and interpret the spectrum using both line intensity ratios and simple broadband model fits. We also present the previously unpublished *ROSAT* High Resolution Imager (HRI) data for W49B—essentially a Si emission-line image through the combined effect of the narrow 0.2–2.2 keV bandpass of the HRI and interstellar absorption of the W49B spectrum at energies below ~ 1 keV. On the basis of our new results, we suggest emission from multiple thermal components as an alternative to the stratification scenario of Fujimoto et al. (1995). As discussed later, however, our results do still allow for the possible spatial separation of Fe from other elements.

After the submission of this paper, we were made aware of a similar analysis of these data reported by Sun & Wang (1999). Our independent analyses lead to similar general conclusions.

For completeness, we note that the remnant displays a sharply defined but incomplete radio shell of radius $\sim 100''$, with high surface brightness and very low polarization (Moffett & Reynolds 1994 and references therein). Based on H I absorption measurements in the radio, the distance to the remnant is 8 ± 2 kpc (Radhakrishnan et al. 1972; adjusted for a Galactocentric radius of 8 kpc, following Moffett & Reynolds 1994). To our knowledge, no optical emission has been reported for this remnant, and it is likely that any such emission is highly absorbed because of W49B's large distance through the Galactic plane. Absorption is virtually negligible for infrared emission, however, and *IRAS* detected strong emission from the vicinity of the remnant (Saken, Fesen, & Shull 1992). Although W49B is probably a young remnant, its infrared colors are more

[1] Laboratory for High Energy Astrophysics, NASA Goddard Space Flight Center, Greenbelt, MD 20771.
[2] Department of Astronomy, University of Maryland, College Park, MD 20742.
[3] Department of Physics and Astronomy, Rutgers University, 136 Frelinghuysen Road, Piscataway, NJ 08854-8019.

TABLE 1

ASCA OBSERVATIONS

Date	Sequence Number	CCD Mode	SIS0 Exposure (ks)
1993 Apr 24.....	50005000	4	20.1
		2	21.8
1993 Oct 16.....	50005010	4	9.2
1993 Oct 17.....	50005020	4	13.7
1993 Nov 3	10020000	1	11.1
1993 Nov 3	10020010	1	17.3
Total			93.2

consistent with an older rather than a young remnant. It is possible that this is in part due to source confusion in a crowded region.

2. DATA REDUCTION

ASCA (Tanaka et al. 1994) features two Solid-State Imaging Spectrometers (SIS0 and SIS1) and two Gas Imaging Spectrometers (GIS2 and GIS3), each with a dedicated mirror. The point-spread function (PSF) of each of the X-ray mirrors has a narrow core of about 1′ FWHM and a half-power diameter of 3′. Each SIS is a square array of four CCD chips, of which 1, 2, or all 4 may be exposed at a time (1-, 2-, or 4-CCD mode). The SIS provides moderate-resolution spectra between the energies of 0.5 and 10 keV, with the best instrument performance in 1-CCD mode ($\Delta E \sim 1/\sqrt{E} \sim 2\%$ at 6 keV at satellite launch in 1993). Because we focus on the line emission in this paper and the GIS provides lower spectral and spatial resolution data than does the SIS, we do not present the GIS data.

There are 10 *ASCA* observations of W49B, all taken in 1993 during the performance verification phase of the mission. The source was observed in a variety of instrument modes and detector positions because it was used as a gain calibrator for the mission. We examine five of the observations in detail; we do not present the other five because they have exposure times shorter than 3 ks, and in all but one, the source is also either off or near the edge of the SIS field of view. Our observations are in different SIS instrument modes (1-, 2-, and 4-CCD), as noted in Table 1, with the source at different positions on the detector.

Since the instrument performance and calibration for the early observations are good, we use the REV2 cleaned data taken directly from the HEASARC archive. Interested readers may consult the *ASCA* Data Reduction Guide (Day et al. 1997) for technical information on the data processing procedures. We focus on the 20 ks 2-CCD mode observation because it has the longest exposure time at a single source position. For fitting line intensities, we also consider a combined SIS spectrum in which all the pulse-height spectra, response matrices, and effective areas are weighted by the exposure time and averaged. We optimize the signal in the high-energy spectrum by taking all the spectra from a

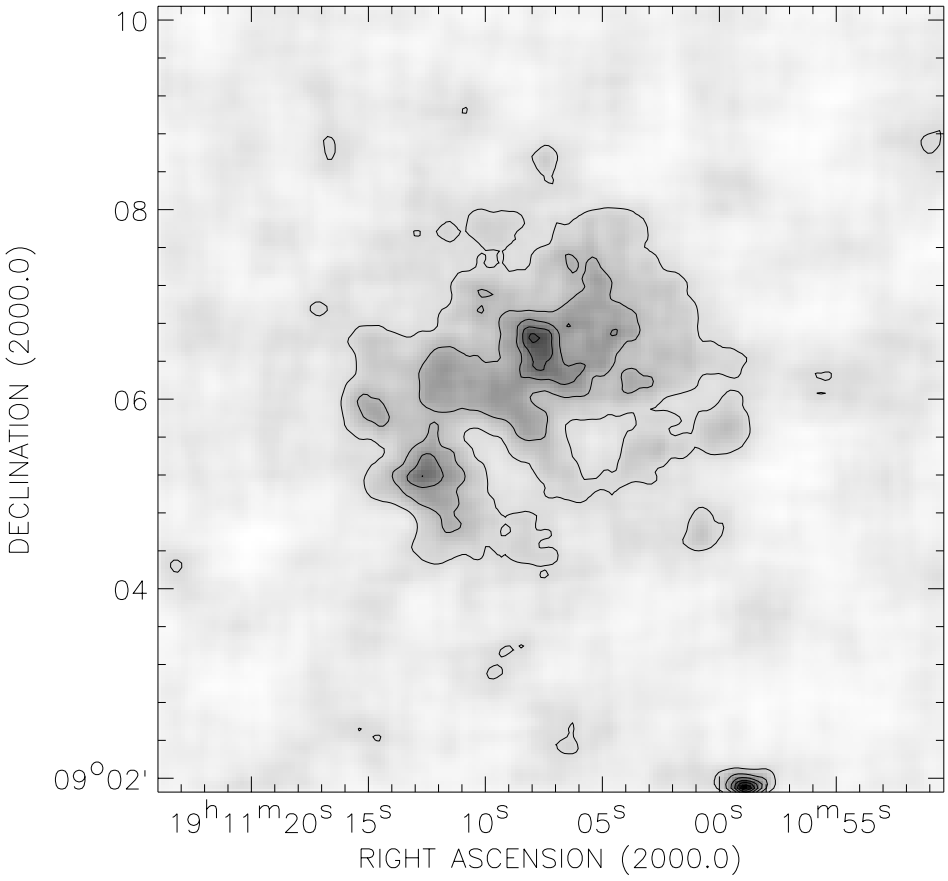

FIG. 1.—Smoothed *ROSAT* HRI image of W49B with contours overlaid corresponding to 0.6, 1.2, 1.9, 2.6, 3.2, and 3.9 × 10^{-3} counts s^{-1} $arcmin^{-2}$. The *ROSAT* image is dominated by the Si emission and shows two brighter spots surrounded by fainter diffuse emission without signs of limb brightening at the 100″ radius of the radio shell.

3.2 radius region centered on the source. This region contains roughly 75% of the total flux from the source.

The background is taken from blank sky fields provided by the *ASCA* Guest Observer Facility. Since W49B is in the Galactic Ridge, we have also verified that the results are not sensitive to the exact background used. We have compared the SIS0 2-CCD mode results using the blank sky field with those using a local background taken away from the source at the edges of the SIS and find very good consistency. The only substantial differences are between the best-fit line intensities of the weak Fe features beyond the strong Fe K blend, but the 90% confidence error ranges are in good agreement. Roughly 80% of the total SIS counts at energies above 1.5 keV come from the source using either background subtraction.

The *ROSAT* HRI has a bandpass of 0.2–2.2 keV and provides a spatial resolution of 5″ at the center of its 38′ wide field of view. A 34 ks observation (*ROSAT* sequence rh500098n00) centered on W49B was processed with software provided by Snowden & Kuntz (1998)[4] to correct for vignetting and to model and subtract the particle background (Snowden 1998). The image shown in Figure 1 is smoothed using an adaptive filter with a varying spatial scale corresponding to 50 counts beam^{-1}. W49B is a weak *ROSAT* HRI source ($\sim$0.05 HRI counts s^{-1}) because the high column density effectively cuts off the spectrum below 1 keV. Compared to the *Einstein* HRI, the *ROSAT* HRI has higher sensitivity and lower background but a narrower bandpass. The two bright spots that dominate the *Einstein* HRI image (Pye et al. 1984; Seward 1990) are clearly seen in the *ROSAT* image, but the *ROSAT* image also shows the surrounding diffuse emission more clearly. The diffuse emission appears to be interior to the radio shell and shows no sign of limb brightening.

[4] ftp://legacy.gsfc.nasa.gov/rosat/software/fortran/sxrb.

3. SPECTRAL RESULTS

We discuss the *ASCA* spectral results for W49B in this section, treating the line intensities and plasma diagnostics first, followed by the fitting of simple broadband spectral models.

3.1. *Line Spectrum*

W49B boasts one of the most impressive emission-line spectra obtained by *ASCA*, featuring prominent Heα blends ($n = 2 \rightarrow n = 1$ in the He-like ion) and Lyα transitions ($n = 2 \rightarrow n = 1$ in the H-like ion) of Si, S, Ar, and Ca, clearly discernible higher level transitions ($1s3p \rightarrow 1s^2$ [hereafter $3p$], $1s4p \rightarrow 1s^2$ [hereafter $4p$]), and a prominent Fe K blend. The line fluxes may be measured by modeling the continuum and fitting narrow Gaussian functions for each distinct emission feature. Figure 2 shows the spectrum combining all the SIS data with the best-fit line model (to be described below).

Line blending can be a significant issue when measuring line fluxes with a moderate resolution spectrometer like the SIS. Two important instances of line blending that we address involve the Lyβ and the $3p$ and $4p$ transitions. At the *ASCA* SIS resolution, Lyβ lines are often blended with the Heα emission of a higher atomic weight element and can have a nonnegligible flux if the corresponding Lyα lines are strong. At the temperature of the W49B continuum ($kT \sim 2$ keV), the ratio of Lyβ to Lyα intensity is between 0.11 and 0.14 for Si, S, and Ar in the models of Raymond & Smith (1977, hereafter RS). For example, in W49B, this means that S Lyβ is responsible for about 25% of the flux that would have been attributed to Ar Heα. In our fits, we therefore

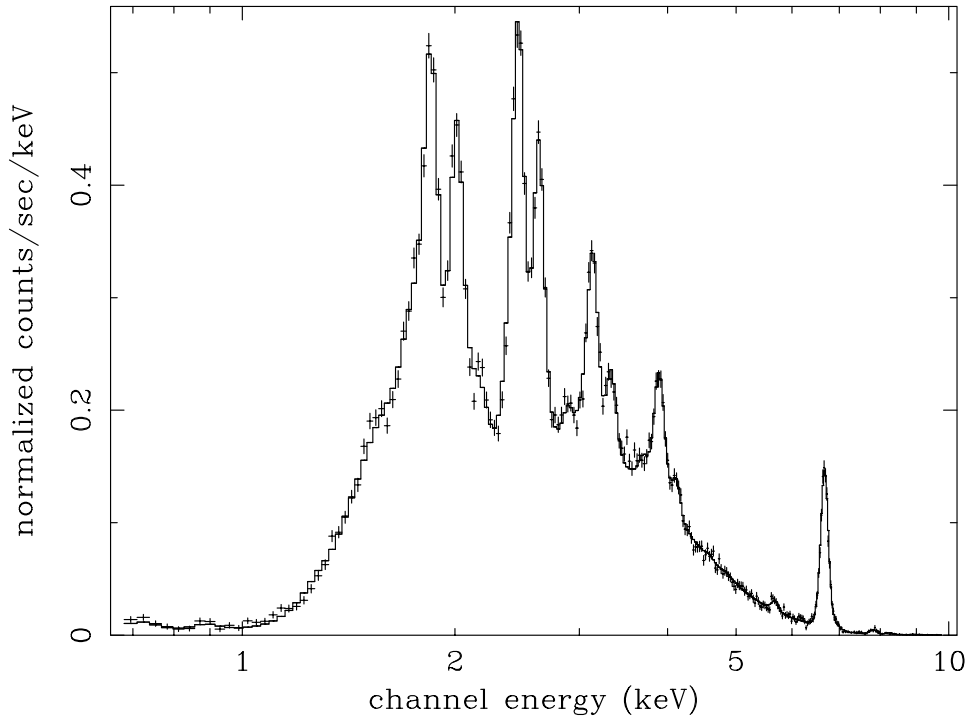

FIG. 2.—Combined SIS data for W49B overlaid with the best-fit ad hoc spectrum for the continuum and lines. This impressive spectrum features prominent emission lines of Si, S, Ar, Ca, and Fe.

include the Lyβ lines of Si, S, and Ar at their expected energies with an appropriately fixed intensity relative to the Lyα line. The $4p$ transition is also sometimes blended with other lines, but fortunately, its intensity relative to the $3p$ transition does not change strongly with temperature and is constant with ionization age. We therefore model the $4p$ line with an intensity relative to $3p$ fixed at 0.6, as is appropriate for temperatures between 1 and 2 keV in the RS models. For Fe, we note that $3p$ is blended with the Heα transitions of Ni at the *ASCA* resolution and that its true flux is overestimated since we do not model the Ni lines.

The energy scale of the W49B spectrum is established by its strong Lyα lines, since they are effectively single transitions at known energies. The measured Lyα energies are in excellent agreement with the expected values, with formal 90% confidence errors that are well within the nominal estimated 0.5% accuracy of the SIS gain; for Ca Lyα, the formal error is comparable to the nominal gain accuracy. In our final fits, we fixed the energies of the Lyα lines at their expected values and adjusted the overall gain of the spectrum by 0.25%. The line energies of the Heα blends are always freely fitted because they depend on the ionization state of the gas: not only do the relative intensities within the triplet of the He-like ion depend on the ionization state, but ions less ionized than the He-like stage may also make a significant contribution to this blend through lines with lower energies. This centroid is thus potentially a valuable diagnostic.

We fitted both the 2-CCD mode SIS0 spectrum and the spectrum combining all the SIS data at energies between 0.6 and 10 keV with a model for the continuum and the line features. Lines of Si, S, Ar, Ca, and Fe were included as described above, and their fitted energies (for Heα) and intensities are given for the combined SIS data in Table 2 with their 90% confidence ($\Delta\chi^2 = 2.71$) errors. The continuum was modeled as two bremsstrahlung components, with temperature about 1.7 keV for the dominant component and fixed at 0.2 keV for the second component. The inclusion of a second continuum component gives a better fit, gives more consistent line diagnostics results, and is consistent with the results of the broadband fits to be described below. The fitted column density is about 5×10^{22} cm^{-2} in the double continuum model, which is significantly higher than the value of 3×10^{22} cm^{-2} when only one continuum component is modeled; the Galactic column density measured in the radio is 1.8×10^{22} cm^{-2} (Dickey & Lockman 1990). The X-ray–measured absorption column density is significantly higher than the radio value, but this appears to be typical for neutral H column densities in excess of several times 10^{20} cm^{-2} because of the presence of interstellar molecular gas (Arabadjis & Bregman 1999). The absolute Si line intensities are therefore significantly different depending how the continuum is modeled, but the Si line intensity ratios discussed below are much less so.

TABLE 2

LINE FLUXES (COMBINED SIS)

Line	Fitted Energy (keV)	Unabsorbed Flux (10^{-3} photons cm^{-2} s^{-1})
Si Heα	1.848 (1.846–1.850)	6.7 (6.5–6.9)
Si Lyα	2.006	3.2 (3.0–3.4)
Si He $3p + 4p$	2.185, 2.294	0.15 (0.05–0.22)
S Heα	2.455 (2.453–2.457)	2.1 (2.0–2.25)
S Lyα	2.623	1.3 (1.2–1.35)
S He $3p + 4p$	2.884, 3.033	0.16 (0.11–0.20)
Ar Heα	3.136 (3.131–3.141)	0.32 (0.30–0.35)
Ar Lyα	3.323	0.19 (0.17–0.21)
Ar He $3p + 4p$	3.685, 3.875	0.067 (0.043–0.090)
Ca Heα	3.880 (3.874–3.887)	0.22 (0.20–0.25)
Ca Lyα	4.105	0.069 (0.057–0.080)
Ca He $3p + 4p$	4.582, 4.818	0.011 (<0.023)
Fe Kα	6.658 (6.656–6.661)	0.83 (0.81–0.86)
Fe Lyα	6.965	0.024 (0.013–0.037)
Fe He $3p + 4p$	7.798, 8.216	0.074 (0.048–0.096)

3.2. *Plasma Diagnostics*

Measured line intensity ratios and Heα centroid energies can provide joint constraints on the emission-averaged temperature and ionization age if the lines are chosen to eliminate or minimize other dependences, such as element abundances or interstellar absorption. The ionization age—defined as $n_e t$, where n_e is the ambient electron density and t is the time since the gas was shock-heated—parameterizes the ionization state of the gas (Gorenstein, Harnden, & Tucker 1974). Gas that is suddenly heated by the passage of the supernova shock wave is ionized slowly through electron-ion collisions on a timescale $10^4/n_e$ yr, where n_e is in cm^{-3}. This timescale may be comparable to, or larger than, the known or deduced age of the remnant for a typical ambient density of 0.1 cm^{-3}; most remnants are therefore expected to not be in ionization equilibrium. Since nonequilibrium ionization (NEI) affects the ion population and line intensities are directly proportional to the population of the relevant ion, it can strongly affect X-ray line intensities. We calculate line emissivity ratios to compare with the observations for a grid of temperatures and ionization ages using the updated code of RS for the X-ray emission and the matrix diagonalization code of Hughes & Helfand (1985) for the nonequilibrium ion fractions.

In Figure 3, we show the constraints on kT and nt based on 90% confidence limits for both the Lyα/Heα and the He $(3p + 4p)$/Heα intensity ratios. Separate panels show the results for each of the elements Si, S, Ar, Ca, and Fe. The observed line intensity ratios are taken from the fit to the combined SIS data with 90% limits determined from the two-dimensional $\Delta\chi^2 = 4.61$ contours. These limits are consistent with, but significantly tighter than, those from the 2-CCD mode SIS0 fits. The values of kT and nt allowed for Ar, Ca, and Fe are consistent with each other near ionization equilibrium at $kT = 2.2$–2.7 keV, with the exception that the Ca He $(3p + 4p)$/Heα ratio is marginally low. Considering that we have not included systematic uncertainties in our errors, the agreement between these three elements is very good, as shown by the overlaid contours in the last panel of Figure 3. The temperature is somewhat higher than the temperature of 1.7 keV inferred for the bremsstrahlung continuum. For the elements Si and S, however, the ratios are inconsistent with each other as well as with the results for Ar, Ca, and Fe. Since it is not possible for any single spectral component to simultaneously reproduce the line ratios for either Si or S, the emission from these elements must be more complex. For Si, this conclusion is supported by the Si Heα line centroid. Its constraints are inconsistent with those from the ratio Si Lyα/Heα, although a 0.5% systematic error on the line energy allows a small region of overlap near collisional ionization equilibrium (CIE; see Fig. 4). The systematic errors on the other centroids are too

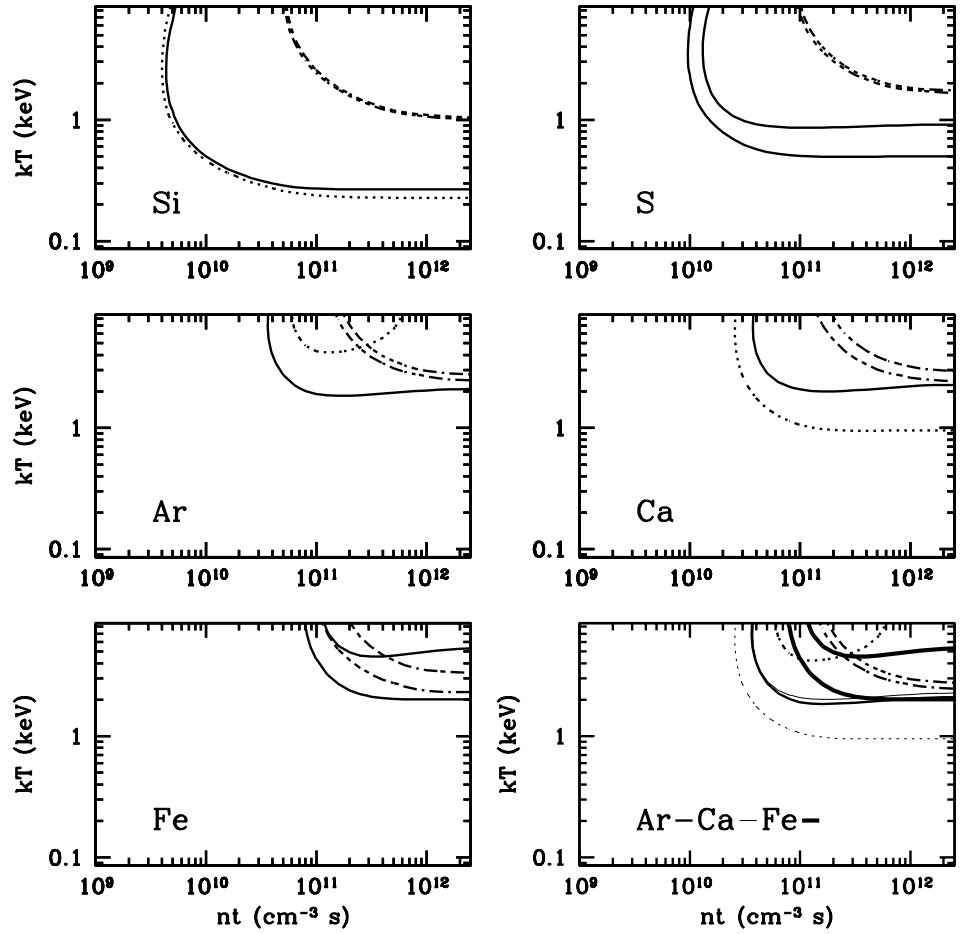

FIG. 3.—Constraints on the emission-weighted average temperature kT (keV) and ionization age nt (cm^{-3} s) in W49B for the elements Si, S, Ar, Ca, and Fe. These are based on ratios of line intensities from the fit to the combined SIS spectrum. Each panel of the figure shows the allowed region of parameter space for one element, as indicated; the last panel shows the regions for Ar, Ca, and Fe overlaid. The region between the two dot-dashed lines (in the upper right of each panel) is consistent with the 90% confidence lower and upper limits for the Lyα/Heα intensity ratio. The solid lines show the region of parameter space allowed by the limits for the He ($3p + 4p$)/Heα ratio. In the plots for Si and Ca, the lower limit for this ratio is outside the boundaries of the plot, as is the upper limit for Ar. For these cases, the locus of points traced by the best-fit value is also shown as a dotted line to clarify the region of parameter space allowed by the data. While the ratios of Ar, Ca, and Fe together essentially allow temperatures of 2–2.5 keV with an ionization age at or near CIE, the Si and S ratios are not consistent with these parameters or with each other.

large to confirm the results of the S line intensity diagnostics or to provide any new constraints for the other elements.

If we assume that one spectral component has a temperature of 2.2 keV and is at CIE, we may then infer parameters characterizing the second component. While the 2.2 keV CIE component gives the wrong Si centroid, the kT and nt values that do give the observed Si centroid also give low Lyα and He $3p + 4p$ intensities relative to the Heα intensity. Thus, the second component could reproduce the Si Heα centroid and provide nearly all of the Si Heα intensity while contributing relatively little to Lyα or He $3p + 4p$. Because of its low temperature, this component contributes less to the S emission and almost nothing to the emission of the other elements. The broadband fits described below confirm that the single-temperature CIE model that accounts for most of the W49B spectrum is deficient in Si Heα flux.

Our results may be compared to the earlier results of Fujimoto et al. (1995), who carried out a similar analysis for W49B using the same data. They use primarily the Lyα/Heα line intensity ratios for Si, S, Ar, and Ca and, as noted earlier, conclude that each of these elements has a different ionization age for a given temperature, with the Si and S parameters being the most disjoint. We are able to reproduce their results by modeling the spectrum with one continuum component and not including weaker lines in the model. When we account for the Lyβ lines, however, we find very good consistency between the parameters for Ar, Ca, and Fe. We also show that the Si and S emission requires multiple spectral components: their line ratios (and the Si centroid) are strongly inconsistent with a single temperature and ionization state. We conclude that the spectral data do not necessarily require stratification of the individual elements, as Fujimoto et al. concluded, but that they do reveal the spectral complexity of the emission from the elements Si and S.

3.3. *Evidence for Emission from* Cr *and* Mn

As the spectral resolution and efficiency of X-ray spectrometers continue to improve, it becomes feasible to search for emission from elements other than the dozen most abundant ones that are now routinely included in spectral models. In Figure 5, the combined SIS spectrum of W49B between the energies 5.0 and 6.4 keV shows linelike features at energies of $\sim$5.7 and 6.1 keV. There are no emission lines in the RS model within the 90% confidence errors of the

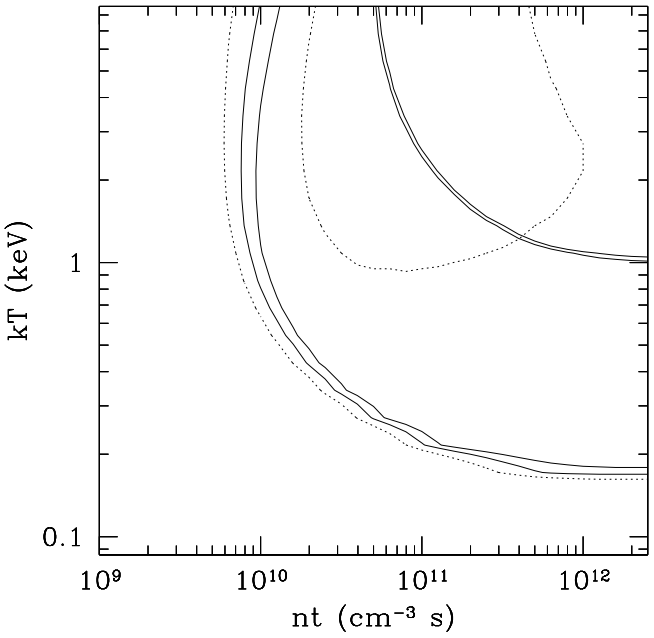

FIG. 4.—Constraints on the temperature and ionization age *nt* of the Si in W49B based on 90% limits for the line ratio Lyα/Heα (*two solid lines in the upper right*) and the Heα centroid (*solid lines in the lower left*). The dotted lines show 0.5% systematic uncertainties in the centroid. The inconsistency between these diagnostics reinforces the conclusions drawn from Fig. 3.

centroids, but these models do not include the elements Cr and Mn. Emission lines of Cr and Mn do have energies near those of the observed line features. The forbidden and resonance transitions of He-like Cr are at 5.655 and 5.682 keV, respectively, and those of Mn at 6.151 and 6.181 keV; the Lyα transitions of Cr and Mn are at 5.917 and 6.424 keV, respectively.

The fluxes and centroids of these features were determined by modeling each as a Gaussian component along with a bremsstrahlung continuum for the portion of the spectrum between energies of 4.5 and 6.4 keV. The lower energy feature, which we tentatively attribute to Cr, appears at a line energy of $5.685^{+0.020}_{-0.027}$ keV and has a flux of $3.0^{+0.8}_{-1.1} \times 10^{-5}$ photons cm^{-2} s^{-1}, corresponding to an equivalent width of about 90 eV. For the other feature, attributed tentatively to Mn, the line energy and flux are $6.172^{+0.047}_{-0.049}$ keV and $1.3^{+1.4}_{-0.6} \times 10^{-5}$ cm^{-3} s^{-1}, or an equivalent width of 60 eV. The reduction in χ^2 from adding the "Cr" feature is more than 20 for 61 degrees of freedom, while the reduction in adding "Mn" is an additional 10. An F-statistic of greater than 10 for 2 and 60 degrees of freedom gives a probability greater than 99% that these features are real.

There are no atomic data currently available for the calculation of emissivities for either Cr or Mn. To check if the strengths of the observed features are consistent with our interpretation of them, we have carried out the tests summarized in Figure 6. We calculate the intrinsic Heα emissivity for Si ($Z = 14$), S ($Z = 16$), Ar ($Z = 18$), Ca ($Z = 20$), Fe ($Z = 26$), and Ni ($Z = 28$) for the 2 keV CIE component without including factors for the element abundances. The crosses in the top panel of the figure show these calculated emissivities plotted against atomic number, overlaid with a spline fit through the individual points. The calculated emissivities are then used with the measured Heα line fluxes to estimate the element abundances for Si, S, Ar, Ca, Fe, and Ni (we use the Fe $3p + 4p$ flux as an upper limit for the Ni Heα flux). These abundances are plotted in the bottom

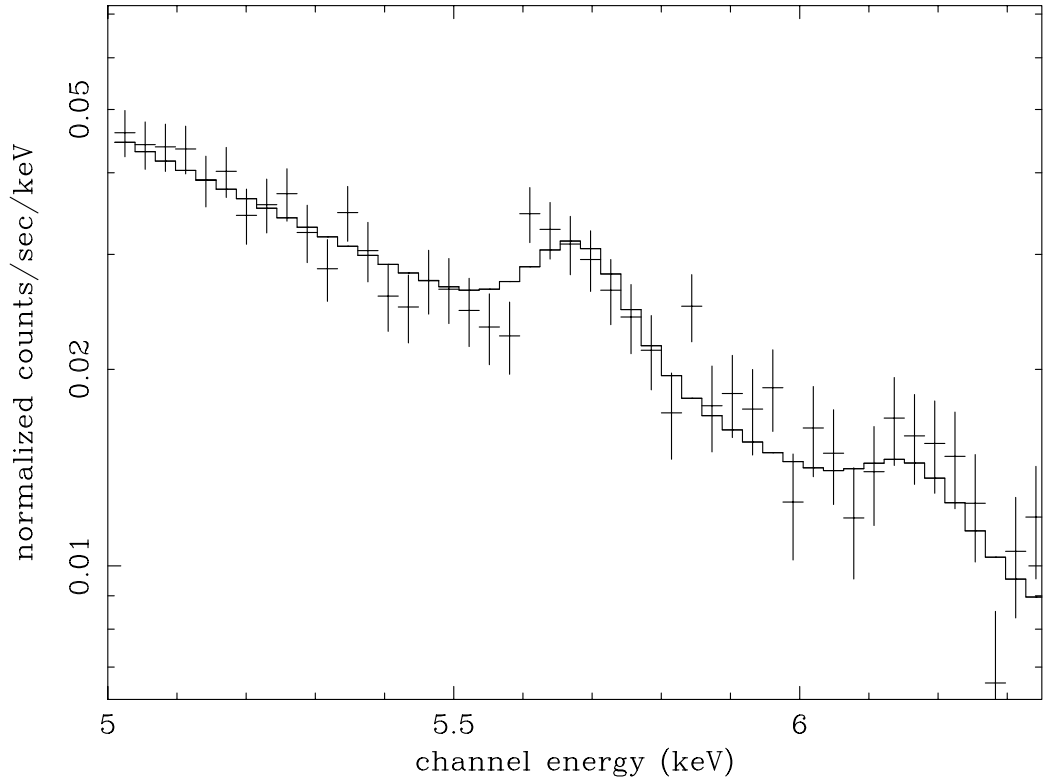

FIG. 5.—Portion of the combined SIS data for W49B with a model for a bremsstrahlung continuum fitted between 4.5 and 6.4 keV and two Gaussian line features overlaid. The fitted line energies and equivalent widths are 5.685 and 6.172 keV and roughly 90 and 60 eV. We identify the line features with Cr and Mn emission.

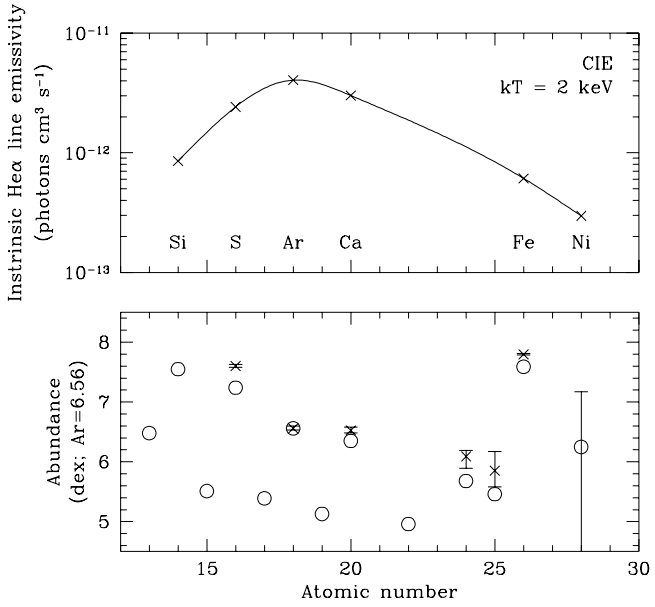

FIG. 6.—*Top panel*: Crosses give intrinsic emissivities (not including element abundance factors) for the Heα blends of Si (atomic weight $Z = 14$), S ($Z = 16$), Ar ($Z = 18$), Ca ($Z = 20$), Fe ($Z = 26$), and Ni ($Z = 28$), calculated with the RS code for the 2 keV CIE component of W49B. The line is a spline fit to these points. *Bottom panel*: Crosses show abundances (normalized to Ar) calculated by using the emissivities in the top panel and the measured Heα line fluxes in W49B. See the text for more discussion. For Cr ($Z = 24$) and Mn ($Z = 25$), the emissivities were interpolated from the curve in the top panel and all the flux at 5.7 and 6.1 keV, respectively, attributed to the Heα blend. The solar photospheric abundance ratios of Anders & Grevesse (1989) are also shown as the circular points to show that the implied abundances for Cr and Mn are consistent with a solar ratio.

panel of the figure as crosses with error bars after normalizing to the Ar abundance. Ar was chosen for the normalization as the lowest atomic number element for which most of the emission comes from the CIE component. We expect both Si and S to have additional emission from a soft component; the high abundances of Si and S (Si is off the scale of the plot) are spurious since their Heα emission arises in part from a cooler NEI component (see § 3.4). For the elements Cr ($Z = 24$) and Mn ($Z = 25$), we interpolate the emissivities using the curve in the top panel of the figure and attribute all the measured flux at 5.7 and 6.1 keV to the Cr and Mn Heα blends, respectively. The resulting abundances are also plotted in the figure as crosses. They are seen to be consistent with the solar photospheric ratios (Anders & Grevesse 1989), which are plotted for each element as open circles in the same panel. As Cr, Mn, and Ni are the next most abundant elements with K-shell emission lines at energies above ~ 4 keV, they are thus the atomic species most likely to be detected next.

3.4. *Broadband Spectral Fitting*

We turn next to fitting of the broadband *ASCA* spectrum of W49B. We use CIE models of RS, NEI models for Sedov hydrodynamics of Hamilton, Sarazin, & Chevalier (1983, hereafter HSC), and single-temperature, single ionization age models of RS with ion fractions calculated according to Hughes & Helfand (1985)—the model used for the line diagnostics (§ 3.2). We expect that at least two spectral components will be required and first verify that no single spectral component provides an adequate fit. An RS model with temperature near 1.7 keV does best, but severely underpredicts the flux of the Si Heα blend and gives χ^2 per degree of freedom greater than 3. A comparable fit is obtained with an NEI model with a similar temperature and an ionization age near 8×10^{11} cm^{-3} s. Most of the X-ray emitting plasma in W49B is clearly at or near CIE, as was first suggested by Smith et al. (1985) based on the Fe K centroid and the Lyα to Kα intensity ratio for the measured continuum temperature of 1.8 keV. The HSC Sedov models do much worse than the other NEI models because the grid of models available to us does not extend sufficiently close to CIE for the relevant temperatures.

We obtain a satisfactory fit to the overall spectrum by combining a CIE RS component with a low-temperature NEI component. Using a HSC Sedov model for the NEI component gives the results shown in Table 3 and Figure 7. The HSC component contributes significantly to the emission lines of Si and S (providing nearly all of the Si Heα blend) and to the surrounding continuum, but little at higher energies. As a Sedov model, it is itself intrinsically multitemperature. If, instead, a single-kT, single-nt model is used for the NEI component, it contributes primarily to the Si Heα blend and very little to other lines. Its contribution to the spectrum falls off more quickly with energy than for the Sedov component, and its parameters are less well constrained. Models with low temperatures between roughly 0.2 and 0.5 keV give good fits for a range of ionization ages consistent with those required to give the observed Si Heα centroid. If two NEI components are used to model the spectrum, CIE is still favored for the dominant component, with a $\Delta\chi^2 = 2.7$ range for $nt > 10^{12}$ cm^{-3} s.

Although the absolute abundances of the elements are model dependent, it is worth examining the abundance results of our simple model fits. To limit the number of free parameters in the models, we linked element abundances together where possible. The CIE component contributes strongly to the line emission from Si, S, Ar, Ca, and Fe, so the abundances of these elements are fitted freely for this

TABLE 3

BROADBAND FIT (2-CCD MODE SIS0)

Parameter	Value
χ^2, dof	219.7, 163
N_H (10^{22} cm^{-2})	5.0 (4.8–5.3)
CIE Component	
kT (keV)	2.0 (1.9–2.1)
EM ($n_e n_H V/4\pi d^2$) (cm^{-5})	4.9 × 10^{12}
Unabsorbed flux (0.5–10. keV) (10^{-10} ergs cm^{-2} s^{-1})	1.5
Mg ($_\odot$)	0 (<1.7)
Si ($_\odot$)	5.0 (3.7–7.0)
S ($_\odot$)	6.4 (4.9–8.5)
Ar ($_\odot$)	7.1 (5.4–9.5)
Ca ($_\odot$)	7.0 (5.5–9.0)
Fe ($_\odot$)	4.8 (4.0–5.8)
Ni ($_\odot$)	14.9 (7.4–23)
HSC NEI Component	
$\langle kT \rangle$ (keV)	0.15
$\langle nt \rangle$ (10^{11} cm^{-3} s)	5.3
Unabsorbed flux (0.5–10. keV) (10^{-10} ergs cm^{-2} s^{-1})	90
Si ($_\odot$)	2.8 (2.1–3.9)
Fe ($_\odot$)	0.9 (0.2–1.6)

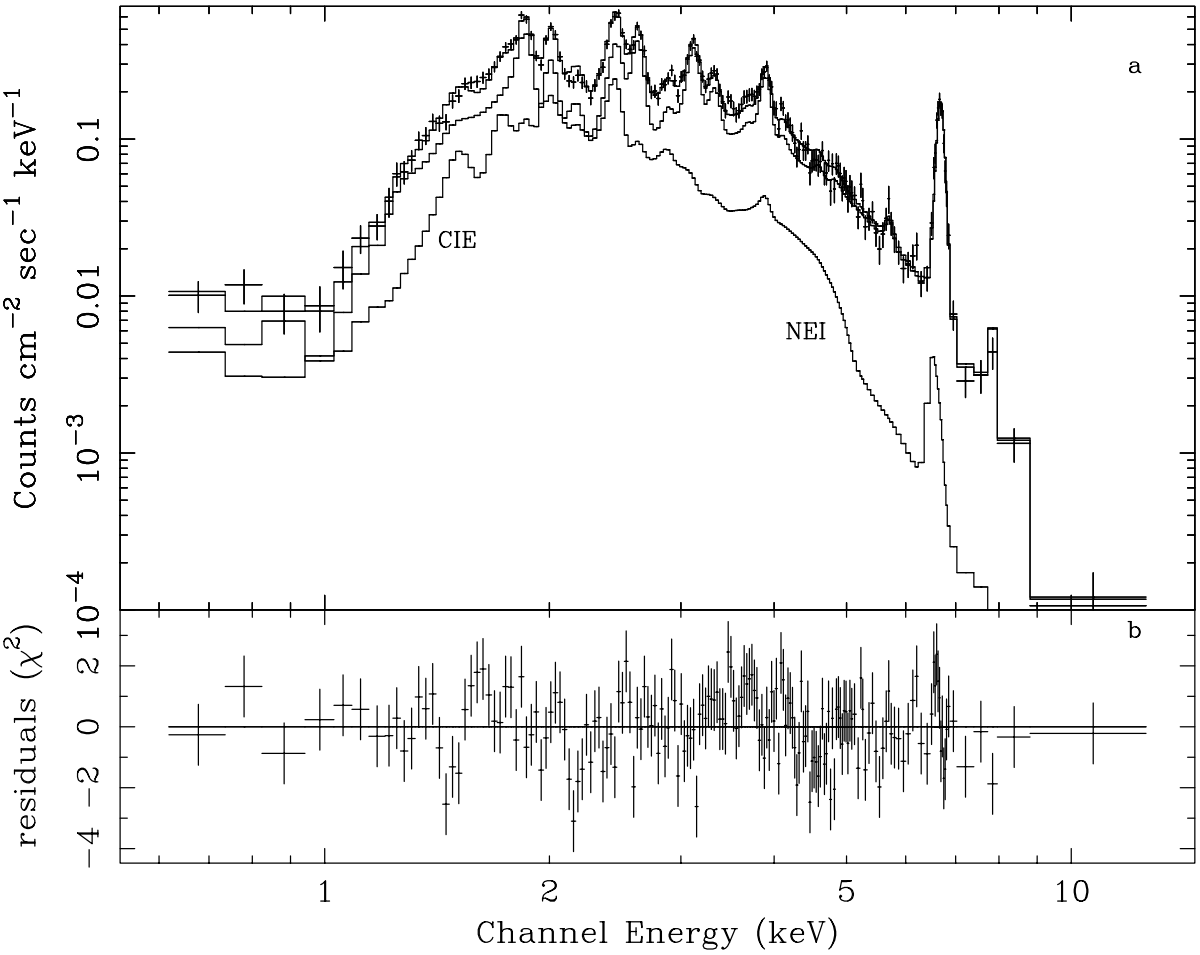

FIG. 7.—Best-fit two-component model to the 2-CCD mode SIS0 spectrum of W49B, folded through the instrument response and overlaid on the data. The model includes a CIE component at temperature $kT = 2.0$ keV and a Sedov NEI component with a shock temperature $kT = 0.15$ keV and ionization age $nt = 5.3 \times 10^{11}$ cm^{-3} s. Each component is also shown separately. The soft NEI component falls off more rapidly with energy, but contributes nearly all of the Si Heα flux, while the CIE component provides most of the flux in the other emission lines. The Cr feature at 5.708 keV has also been included. See the text for further discussion.

component. The Mg and Ni abundances are also fitted because Mg and Fe L emission are blended together at energies near 1.3 keV, with the Fe L atomic data having known deficiencies (Liedahl, Osterheld, & Goldstein 1995) while Ni and Fe emission are blended together at energies near 7.8 keV. The abundances of C, N, O, and Ne are fixed at their solar value—a sufficient assumption since this spectrum is strongly attenuated by absorption at the relevant energies below about 1 keV. The data cannot constrain a second full set of abundances for the NEI component, so the C, N, O, Ne, and Mg abundances are fixed at their solar value, Si through Ca tied to their solar ratios, and Fe tied to Ni. The abundance results are summarized in Table 3. The primary CIE component requires abundances for Si, S, Ar, Ca, and Fe that are comparable to each other and significantly enhanced above the solar value. The Mg abundance is formally zero, but has a large error. The second, NEI component suggests an enhanced Si abundance and a rather low Fe abundance, but these abundances are nearly consistent when their errors are considered (see Table 3).

4. DISCUSSION

The results of the broadband fits indicate that the X-ray emission from W49B is dominated by its ejecta and that the ejecta are at or very near CIE. Ejecta-dominated remnants are expected to be dynamically young, so a high ionization age requires a high density. We obtain a lower limit for the internal density of the X-ray–emitting gas of 2 cm^{-3} by using the X-ray emission measure for the CIE component and assuming that it fills a sphere with the radius of the radio shell. The same value was obtained by Smith et al. (1985) from the *EXOSAT* X-ray data. Moffett & Reynolds (1994) also cite this value as the minimum density required for significant Faraday depolarization of the radio emission. The high density required to explain the X-ray emission thus also allows a possible explanation for the unusually low polarization in the radio. The actual density would need to be even higher since the X-ray emission does not appear to fill the radio shell and is clearly centrally concentrated. The high density places constraints on the properties of the progenitor. Massive progenitors of type O through B0 clear a surrounding radius of 15 pc during their main-sequence lifetime through their fast stellar winds and photoionizing radiation (e.g., Chevalier 1990). These progenitors do not seem plausible for W49B, which has a radius of only about 5 pc for a distance of 8 kpc, unless it is still interacting with dense circumstellar material ejected by a slow wind if the progenitor underwent a red giant phase.

The element abundances are compared with the calculated abundances for various supernova progenitors in

Figure 8. We focus on the relative abundances because we find that they are more consistent among the various models than are the absolute abundances. The 90% confidence limits for the measured abundances of Mg, S, Ar, Ca, Fe, and Ni relative to the abundance of Si in the CIE component are determined from the two-dimensional $\Delta\chi^2 = 4.6$ contours. The calculated abundances for two Type Ia models—the standard W7 model and a delayed detonation model (WDD2)—plus Type II models for progenitor masses of 13 and 15 $M_\odot$ are all taken from Nomoto et al. (1997a, 1997b) and normalized to the Si abundance. All abundances are given relative to the solar photospheric abundances of Anders & Grevesse (1989). As can be seen from the figure, the 90% confidence limit for the Mg abundance relative to Si is consistent with all the Type Ia and low-mass Type II models that we considered. More massive Type II progenitors would produce too much Mg relative to Si to be consistent with the data. All the models underpredict Ar relative to Si, but the Type II models also underpredict S and Ca relative to Si. The WDD2 Type Ia model appears to be favored overall for the CIE component, but is still far from being consistent with all the observations.

Other possible nucleosynthesis diagnostics are the relative abundances of less abundant elements, such as Ti, Cr, and Mn. According to the nucleosynthesis models used for Figure 8, the Ti abundance relative to Mn and Cr is depressed relative to solar in Type Ia explosions, while the three are comparable in low-mass Type II explosions. We demonstrated above that Cr and Mn are in roughly their solar ratio relative to Ar. Our 90% confidence limits on the Ti Heα flux is 2×10^{-5} cm^{-2} s^{-1} at an energy $\sim$4.97 keV

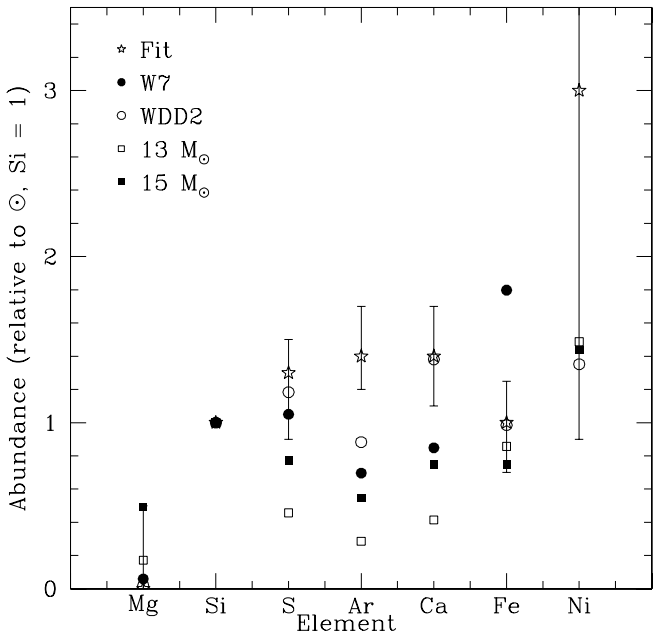

FIG. 8.—Element abundances in the CIE component of the W49B spectral model (*open stars*), normalized to the Si abundance relative to the solar abundances of Anders & Grevesse (1989). The error bars are for 90% confidence ($\Delta\chi^2 = 4.61$ two-dimensional contours). Also shown are the abundances in the Type Ia models W7 (*filled circles*) and WDD2 (*open circles*) and the Type II models for 15 $M_\odot$ (*filled squares*) and 13 $M_\odot$ (*open squares*) progenitors of Nomoto et al. (1997a, 1997b). The Type I models have more success overall, as the Type II models tend to underpredict S, Ar, and Ca relative to Si. All the models appear to predict weaker Ar than is observed.

(the He-like resonance and forbidden transitions of Ti are at 4.966 and 4.977 keV and overlap the He 3*p* and 4*p* transitions of Ca at the *ASCA* resolution). Using Figure 6, the 90% upper limit for the Ti abundance relative to Ar is about 5.7 dex, or a few times the solar value. Thus, our upper limit does not distinguish between the models, but future measurements of these quantities may improve enough to make such diagnostics useful. Foremost is the need for calculated emissivities for these elements so that measured line fluxes can be converted into reliable element abundances. Currently, the codes that calculate X-ray emission do not include the elements Ti, Cr, or Mn.

The total mass of the ejecta may formally be calculated by assuming a geometry for the remnant. The *ROSAT* image is essentially a Si plus continuum image, showing two bright spots plus a shelf of fainter diffuse emission, each contributing roughly half of the image counts. Since the Fe K and hard continuum images of Fujimoto et al. (1995) are less extended than the Si and S images, we conclude that the soft spectral component is more spatially extended and that the hard component comes from the two bright spots. If we assume that the CIE component comes from the two bright lobes and model them as spheres of diameter 0.5, the total mass of the CIE component is 1.6 $M_\odot$. This mass is marginally consistent with the ejecta mass from a Type Ia explosion, but is based on uncertain assumptions about the geometry and the relative abundances of elements that do not exhibit strong emission lines. Our simple mass calculation therefore does not unambiguously differentiate between Type Ia and Type II progenitors. The calculated Si and Fe ejecta masses, at 0.02 and 0.04 $M_\odot$, respectively, are lower than the Si and Fe masses for either Type Ia or Type II explosions. The calculated masses increase if the CIE component is more extended than assumed, and also if the soft NEI component in W49B is associated with ejecta.

Our broadband spectral fit results indicate that the Si and S lines have a significant contribution from the NEI component and that Si Heα in particular comes almost entirely from it. Meanwhile, the Ar, Ca, and Fe K emission comes almost entirely from the hotter CIE component. The *ASCA* images of Fe K and Si from Fujimoto et al. (1995) show a distinct difference in morphology that can be explained naturally if, as we have assumed earlier, the two spectral components that we have identified in W49B have different spatial distributions: a compact component for Fe K and a more extended component for Si. We then expect that the Si Lyα emission should be morphologically similar to the Fe K emission (since both come from the CIE component), while Si Heα should be morphologically different (since it comes from the other, cool NEI component). Fujimoto et al. show that the radial profiles for these two Si lines actually look similar. Since the *ASCA* PSF is not much smaller than the remnant itself and photon statistics are limited for an image of a single line feature, more sensitive and higher spatial resolution observations with *Chandra* and *XMM* will be necessary to resolve these discrepancies. If the distribution of the Si Lyα emission is truly similar to Si Heα and distinct from Fe K, our spectral results would require both cool and hot extended Si ejecta and compact hot Fe ejecta, implying spatial segregation of the Si and Fe ejecta.

It is also possible that the soft spectral component represents a cool blast wave, as suggested by Smith et al. (1985). If so, our Sedov parameters require the explosion to have

been very weak ($E < 10^{50}$ ergs) and the remnant age to be about 4000 yr—conclusions that are qualitatively similar to those reached by Smith et al. We cannot be certain that the soft component is actually the blast wave, however. The soft emission, while extended, is not limb-brightened and does not appear to fill the radio shell in currently available X-ray images. We also obtained better fits with enriched Si abundance than with the element abundances in solar ratios, suggesting that the soft NEI component may be from ejecta, although the models used are in need of updated atomic physics. In any case, forthcoming observations of the distribution of the Si emission will shed much light on this issue. The blast wave may be too faint to have been detected yet.

The *ASCA* X-ray observations have provided a wealth of new information about the unusual supernova remnant W49B. It has a rich and complex spectrum including previously undetected emission lines of the elements Cr and Mn. The remnant shows evidence for spatial differences between the X-ray emission of different elements that are not yet understood; they may be due to ejecta plus the blast wave, which has not yet been positively identified in X-rays, or to ejecta of different densities and spatial distributions. W49B bears the strong imprint of its progenitor in that its X-ray emission is still dominated by its ejecta, but it is also clearly the product of its complex environment. It is an unusual example of an ejecta-dominated remnant wherein much of the gas is very near CIE, indicating that this young remnant has a very dense environment, whether interstellar or circumstellar. The current data and models do not conclusively resolve whether this was a Type Ia or Type II explosion nor whether the soft spectral component is from a cool blast wave or from ejecta, but they have raised tantalizing puzzles and hints of new discoveries that may be solved with future observations. These are fortunately soon forthcoming.

This work was based on archival X-ray data provided by the HEASARC at NASA Goddard Space Flight Center. We thank Steve Snowden for providing software to process the *ROSAT* data. U. H. acknowledges partial support through the NASA Astrophysics Data Program, and J. P. H. acknowledges support through NASA grants NAG 5-4794, NAG 5-4871, and NAG 5-6419.

REFERENCES

Anders, L., & Grevesse, N. 1989, Geochim. Cosmochim. Acta, 53, 197
Arabadjis, J. S., & Bregman, J. N. 1999, ApJ, 510, 806
Chevalier, R. A. 1990, in Supernovae, ed. A. G. Petschek (New York: Springer), 91
Day, C., et al. 1997, The *ASCA* Data Reduction Guide (Greenbelt: NASA/GSFC)
Dickey, J. M., & Lockman, F. J. 1990, ARA&A, 28, 215
Fujimoto, R., et al. 1995, PASJ, 47, L31
———. 1997, AJ, 114, 2058
Gorenstein, P., Harnden, R., & Tucker, W. 1974, ApJ, 192, 661
Hamilton, A. J. S., Sarazin, C. L., & Chevalier, R. A. 1983, ApJS, 51, 115
Hughes, J. P., & Helfand, D. J. 1985, ApJ, 291, 544
Liedahl, D. A., Osterheld, A. L., & Goldstein, W. H. 1995, ApJ, 438, L115
Moffett, D. A., & Reynolds, S. P. 1994, ApJ, 437, 705
Nomoto, K., Hashimoto, M., Tsujimoto, T., Thielemann, F.-K., Kishimoto, N., Kubo, Y., & Nakasato, N. 1997a, Nucl. Phys. A, 616, 79
Nomoto, K., Iwamoto, K., Nakasato, N., Thielemann, F.-K., Brachwitz, F., Tsujimoto, T., Kubo, Y., & Kishimoto, N. 1997b, Nucl. Phys. A, 621, 467
Pye, J. P., Becker, R. H., Seward, F. D., & Thomas, H. 1984, MNRAS, 207, 649
Radhakrishnan, V., Goss, W. M., Murray, J. D., & Brooks, J. W. 1972, ApJS, 24, 49
Raymond, J. C., & Smith, B. W. 1977, ApJS, 35, 419
Saken, J. M., Fesen, R. A., & Shull, M. 1992, ApJS, 81, 715
Seward, F. D. 1990, ApJS, 73, 781
Smith, A., Jones, L. R., Peacock, A., & Pye, J. P. 1985, ApJ, 296, 469
Snowden, S. L. 1998, ApJS, 117, 233)
Sun, M., & Wang, Z. R. 1999, preprint (astro-ph/9911322
Tanaka, Y., Inoue, H., & Holt, S. S. 1994, PASJ, 46, L37
Thielemann, F.-K., Nomoto, K., & Hashimoto, M. 1990, in Supernovae, ed. J. Audoze, S. Bludman, R. Mochkovitch, & J. Zinn-Justin (New York: Elsevier)